Quaternary Science Reviews 189 (2018) 134–148

Contents lists available at ScienceDirect

Quaternary Science Reviews

journal homepage: www.elsevier.com/locate/quascirev

Late Quaternary deglacial history across the Larsen B embayment, Antarctica

Ara Jeong [a], Jae Il Lee [b], Yeong Bae Seong [c, *], Greg Balco [d], Kyu-Cheul Yoo [b], Ho Il Yoon [b], Eugene Domack [e], Hyun Hee Rhee [c], Byung Yong Yu [f]

[a] School of Geographical Sciences and Urban Planning, Arizona State University, Tempe, AZ 85287, USA
[b] Korea Polar Research Institute, Incheon 21990, South Korea
[c] Department of Geography, Korea University, Seoul 02841, South Korea
[d] Berkeley Geochronology Center, 2455 Ridge Road, Berkeley, CA 94709, USA
[e] College of Marine Science, University of South Florida, 140 7th Avenue South, St. Petersburg, FL 33701, USA
[f] AMS Laboratory, Advanced Analysis Center, Korea Institute of Science and Technology, Seoul 02792, South Korea

ARTICLE INFO

Article history:
Received 27 February 2018
Received in revised form
12 April 2018
Accepted 16 April 2018
Available online 24 April 2018

Keywords:
Quaternary
Glaciation
Antarctica
Cosmogenic isotopes
Glacial geomorphology
Larsen ice shelf
Deglaciation
Meteoric ^{10}Be
In-situ ^{14}C

ABSTRACT

We measured meteoric ^{10}Be variation throughout a marine sediment core from the Larsen B embayment (LBE) of the Antarctic Peninsula, and collected in situ ^{10}Be and ^{14}C exposure ages on terrestrial glacial deposits from the northern and southern margins of the LBE. We use these data to reconstruct Last Glacial Maximum (LGM) to present deglaciation and ice shelf change in the LBE. Core sedimentary facies and meteoric ^{10}Be data show a monotonic progression from subglacial deposits to sub-ice-shelf deposits to open-marine conditions, indicating that its collapse in 2002 was unprecedented since the LGM. Exposure-age data from the southern LBE indicate 40 m of ice surface lowering between 14 and 6 ka, then little change between 6 ka and the 2002 collapse. Exposure-age data from the northern LBE show a bimodal distribution in which clusters of apparent exposure ages in the ranges 4.9–5.1 ka and 1.0–2.0 ka coexist near 50 m elevation. Based on these results, other published terrestrial and marine deglaciation ages, and a compilation of sea bed imagery, we suggest a north-to-south progression of deglaciation in the northeast Antarctic Peninsula in response to Holocene atmospheric and oceanic warming. We argue that local topography and ice configuration inherited from the LGM, in addition to climate change, are important in controlling the deglaciation history in this region.

© 2018 Elsevier Ltd. All rights reserved.

1. Introduction

The Antarctic Peninsula experienced rapid regional warming over the last century, with a rise in temperature six times greater than the global mean (Vaughan et al., 2003). Recent sequential north-to south retreat and collapse of Antarctic Peninsula ice shelves including the Larsen A (LAIS) in 1995, the Larsen B (LBIS) in 2002, and current thinning of Larsen C (LCIS) (Shepherd et al., 2003) (Fig. 1) has led to concern about stability of other Antarctic ice shelves and potential sea-level impacts of ice shelf collapse under future warming (Scambos et al., 2003; Shepherd et al., 2003; Rignot et al., 2004; Glasser and Scambos, 2008; Banwell et al., 2013). For example, accelerated glacial flow promoted by the removal of buttressing by the LBIS (De Rydt et al., 2015) triggered mass loss of 27 km^3 yr^{-1} in glaciers across the Larsen B embayment (LBE), which has significantly contributed to global sea level change (Rignot et al., 2004). Bentley (1999) estimated that changes in the ice volume of the Antarctic Peninsula during the postglacial contributed to a rise in global sea level ~ 1.7 m, compared with 6–13 m for the entire Antarctic Ice Sheet, although Shepherd and Wingham (2007) suggested the sea level contribution of the Antarctic Peninsula (AP) is negligible because snowfall-driven growth of continental ice cap in AP would cancel out the accelerated flow from the Larsen A embayment (LAE) and Larsen B embayment (LBE). Thus, for example, the trillion-ton iceberg which broke off from the LCIS on July 12, 2017 has led to concern about the sea-level impacts of potential future disintegration of the LCIS (MIDAS Project, 2017).

The purpose of this study is to gain information about past ice-shelf changes in the Larsen embayment during LGM-to-Holocene

* Corresponding author.
E-mail address: ybseong@korea.ac.kr (Y.B. Seong).

https://doi.org/10.1016/j.quascirev.2018.04.011
0277-3791/© 2018 Elsevier Ltd. All rights reserved.

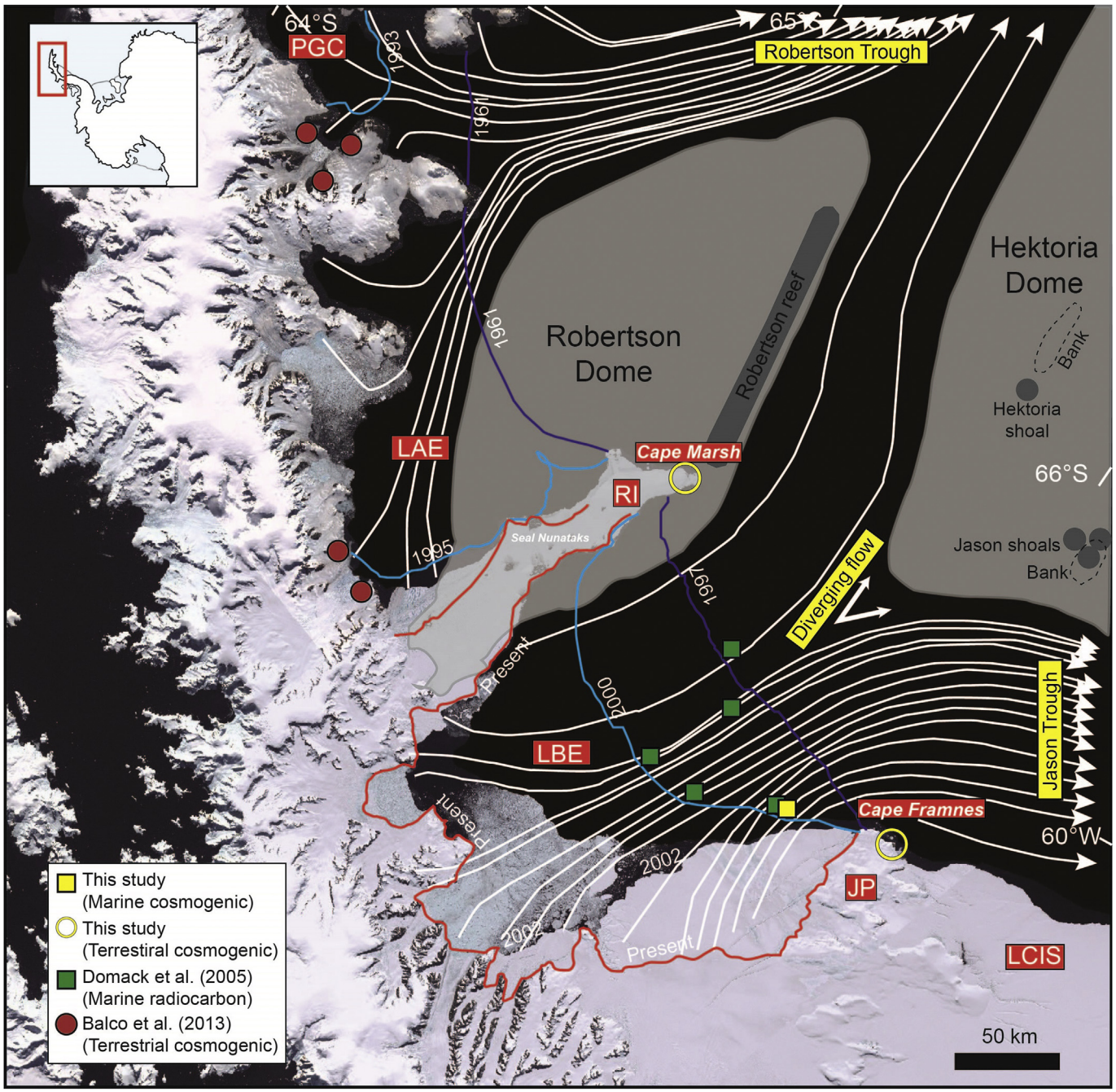

Fig. 1. The Larsen B embayment with coring locations and sampling sites for exposure dating, as well as paleo-ice configurations and flow at the global last glacial maximum (LGM). The background image was obtained from the USGS Landsat Image Mosaic of Antarctica, and the annual coastal line was extracted from the SCAR Antarctic Digital Database. Paleo-ice flow directions and locations of the ice domes are modified from Lavoie et al. (2014). Topographic banks (Sloan et al., 1995) and shoal and reef areas (Lavoie et al., 2014) indicate the shallowest areas of the region which could have worked as centers of glacial nucleation (Lavoie et al., 2014). Abbreviations used: PGC: Prince Gustav Channel; JRI: James Ross Island; LAE: Larsen A embayment; RI: Robertson Island; LBE: Larsen B embayment; JP: Jason Peninsula; LCIS: Larsen C Ice Shelf.

deglaciation that can potentially be valuable in understanding present and future ice shelf change. A complex LGM-to-present history has been reported among the ice shelves of the north-eastern Antarctic Peninsula (NEAP) (Johnson et al., 2011). The LAIS is thought to have collapsed almost completely during the middle to late Holocene, and then re-formed again before the collapse in January 1995 (Brachfeld et al., 2003; Balco et al., 2013), whereas the LBIS is believed to have remained intact throughout the Holocene until its latest collapse (Domack et al., 2005).

In this study we gather geological and geochemical observations that improve our reconstruction of LBIS change and provide some information about the LCIS, including (i) applications of the rare radionuclides ^{10}Be and ^{14}C produced by cosmic-ray interactions both in the atmosphere ("meteoric" ^{10}Be) and in surface rocks and minerals ("in-situ-produced" ^{10}Be or ^{14}C) (Fig. 2); (ii) sedimentological analysis of marine cores, and (iii) a compilation of marine bathymetric data related to ice-flow reconstruction (Lavoie et al., 2014). Meteoric ^{10}Be variations within marine sediment cores reflect the changing extent to which the area is open over time, which, in turn, helps to define the number of ice shelf collapses

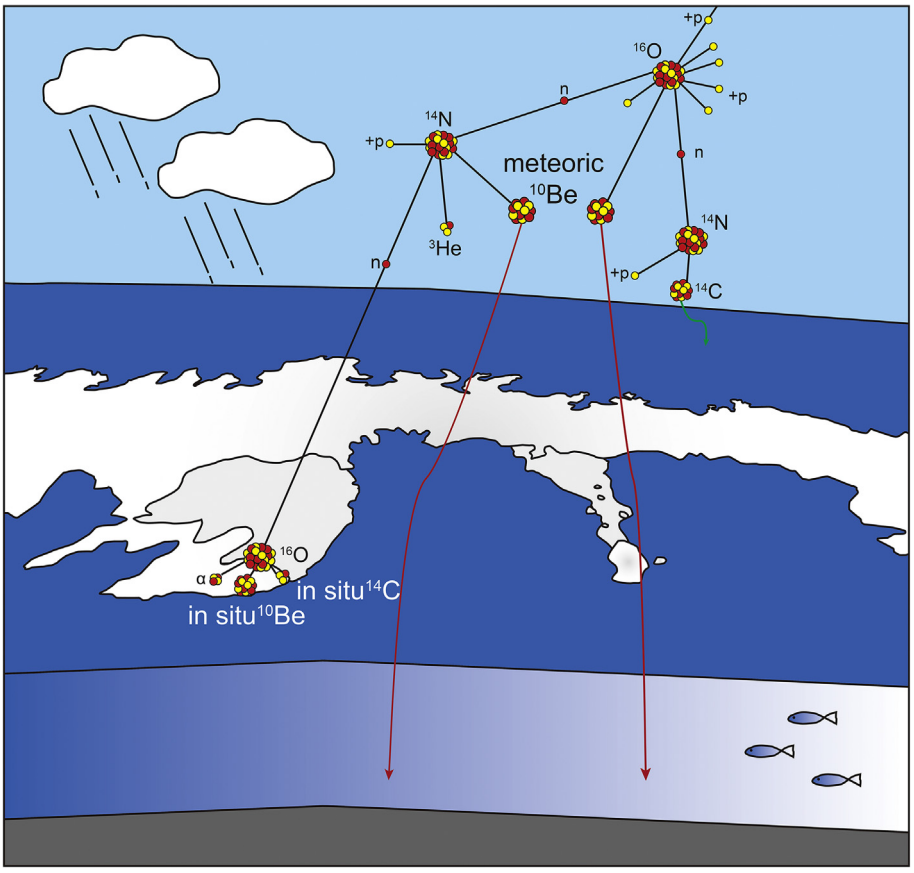

Fig. 2. The pathways for production of meteoric ^{10}Be and in situ ^{10}Be. Meteoric ^{10}Be is produced by spallation in the atmosphere, whereas in situ ^{10}Be is produced in the uppermost few meters of the Earth surface (modified from Willenbring and von Blanckenburg, 2010).

(Scherer et al., 1998). Surface exposure ages derived from *in-situ*-produced ^{10}Be and ^{14}C provide the timing of the initiation of ice thinning and its duration. Paired ^{14}C and ^{10}Be, with different half-lives (5.7 ka and 1.387 Ma), can determine the likelihood of multiple exposure events of any erratics, which commonly occurs due to incomplete removal of prior exposure inheritance under cold-based ice in Antarctica (White et al., 2011; Balco et al., 2013). Thus, we can apply both marine and terrestrial evidence to address changes in both extent and thickness of glaciers and ice shelves during the Holocene.

2. Study area

The Larsen ice shelf is located at the eastern edge of the Antarctic Peninsula (AP) and calves into Weddell Sea (Fig. 1). Prior to 1995, subsections of the Larsen ice shelf called, from north to south, Larsen A (LAIS), Larsen B (LBIS), and Larsen C ice shelf (LCIS), filled three distinct embayments. At present, only small portions of the LAIS and LBIS remain (Evans and Ó Cofaigh, 2003; Evans et al., 2005).

At the LGM, the AP ice sheet grounded on the nearby continental shelf edge. Ice retreat began at the outer shelf at 18.3 kyr (Heroy and Anderson, 2005) and much of the inner shelf was ice-free by 13 kyr (Ó Cofaigh et al., 2002, 2005; Dowdeswell et al., 2004a, 2004b; Heroy and Anderson, 2005; Anderson and Fretwell, 2008). Lavoie et al. (2014) reconstructed the LGM ice configuration based on ice flow directions inferred from multibeam bathymetry showing divergence of flow around several ice domes (Fig. 1). Ice emerging from the Seal Nunataks and Robertson Island moved toward the southeast then eastward toward the Robertson Trough, (Evans et al., 2005), whereas ice in the southern sector diverged to the south, likely overflowing Cape Framnes (Lavoie et al., 2014, Fig. 1). Climate records (Bentley et al., 2009; Davies et al., 2012; Ciais et al., 1992; Masson et al., 2000; Masson-Delmotte et al., 2004) indicate significant warming at the beginning of the Holocene at 11 ka, but there is no evidence for collapse of ice shelves until the Mid-Holocene Climatic Optimum (MHCO) ca. 4.5–3 ka. The Prince Gustav Channel (PGC) ice shelf and LAIS were absent during the MHCO and reformed before approximately 2 kyr and 1.4 kyr, respectively (Brachfeld et al., 2003; Pudsey et al., 2006). However, Domack et al. (2005) demonstrated, based on a comparison of diatom abundance between the LBIS and the LAIS, that the LBIS was continuously present during the Holocene until its 2005 collapse.

In this work we describe terrestrial and marine geologic evidence from the LBE as follows. We collected a marine sediment core (EAP13-GC17: 65° 48.1656′ S, 60° 39.4296′ E, 526 m water depth) collected between the 1997 and 2000 positions of the LAIS edge. We analyze the concentration of meteoric ^{10}Be and ^{10}Be/^{9}Be ratio from the core to investigate the openness of the location after LGM. We collected glacially transported erratics from ice-free areas above sea level at Robertson Island (RI) and Cape Framnes (CF) and applied ^{10}Be and ^{14}C exposure dating to constrain the downwasting history of LBIS.

3. Methods

All cores and terrestrial samples were collected during the KOPRI (Korea Polar Research Institute) Antarctic cruise of the Araon

for the austral summer and fall of 2013. After cutting core EAP13-GC17 into sections and preserving one split for archival purposes, we prepared the second split for onboard analysis. All info on sediments characteristics including lithology, sedimentary texture, structures, bed contacts, clast shape, and grain-size distribution was described on board by E. Domack.

3.1. Meteoric ^{10}Be

A total of 29 samples from a core 2.22 long were taken for beryllium isotope analyses at 8 cm intervals at first, followed by 8 additional samples at intermediate positions where notable ^{10}Be concentration changes took place (Table 1). The samples were dried and grinded for homogenization. The >200 μm fraction was removed and only the <200 μm fraction was processed further to remove size dependency related to chemical adsorption of beryllium. In contrast to observed grain-size dependency of ^{10}Be in previous studies (Shen et al., 1992, 2004; Gu et al., 1996; Maejima et al., 2005; Willenbring and von Blanckenburg, 2010; Graly, 2011), our study shows no significant relationship between ^{10}Be concentration and grain size (Fig. 3).

After oxidization to remove organic materials, we added 0.4 mg of ^{9}Be carrier (~1000 ppm) to 0.5 g of sediment samples and used the potassium bifluoride fusion procedure of Stone (1998), to achieve isotopic equilibrium between ^{10}Be and ^{9}Be. The fusion procedure extracts both authigenic Be (adsorbed to grain surfaces during transport and sedimentation in the marine environment) and detrital Be (present within mineral grains in the sediment prior to introduction to the marine environment). Here we are interested in the authigenic ^{10}Be inventory, that more likely represents the seawater composition compared to the whole sediment (McHargue et al., 2000), so it is necessary to correct total ^{9}Be measurements to exclude detrital ^{9}Be from terrestrial sources assuming detrital ^{10}Be is negligible (<0.1%) compared to the authigenic inventory. To make this correction, we measured both (i) the total ^{9}Be by dissolution of samples in a mixture of HF, HNO_3 and HCl (Bourles et al., 1989) and (ii) the authigenic ^{9}Be concentration by leaching with 0.04M hydroxylamine in 25% acetic acid solution (Bourles et al., 1989). The Be concentration measurements in the resulting solutions were measured by Inductively Coupled Plasma Atomic Emission Spectrometry (ICP-AES) and Mass Spectrometry (ICP-MS). We then compute the authigenic ^{10}Be concentration by multiplying the total

Table 1
The meteoric ^{10}Be and ^{9}Be Data from the core taken from the Larsen B Ice Shelf.

Depth (cm)	Sample mass (g)	Authigenic $^{10}Be/^{9}Be$ ratio (10^{-11})[a]	Total ^{9}Be (ppm)[b]	Detrital ^{9}Be (ppm)[c]	Authigenic ^{9}Be (ppm)[d]	^{10}Be concentration (10^{6} atoms g^{-1})	Decay-corrected ^{10}Be concentration (10^{6} atoms g^{-1})[e]
0	0.503	839.72 ± 9.21	1.69 ± 0.01	0.62 ± 0.03	1.07 ± 0.05	599.17 ± 6.56	599.86 ± 6.58
8	0.507	818.93 ± 8.26	1.89 ± 0.05	0.93 ± 0.05	0.96 ± 0.04	524.52 ± 5.28	525.20 ± 5.29
16	0.501	739.37 ± 7.02	1.68 ± 0.03	0.66 ± 0.06	1.03 ± 0.09	508.43 ± 4.82	509.16 ± 4.83
24	0.507	333.91 ± 4.58	1.77 ± 0.06	0.58 ± 0.07	1.19 ± 0.09	265.79 ± 3.64	266.21 ± 3.65
28	0.517	163.32 ± 3.24	n.m.[f]	n.m.	1.24 ± 0.05	135.39 ± 2.68	135.62 ± 2.69
32	0.514	79.86 ± 7.61	1.55 ± 0.05	0.38 ± 0.04	1.17 ± 0.02	62.47 ± 5.95	62.59 ± 5.97
36	0.513	27.72 ± 0.78	n.m.	n.m.	1.33 ± 0.03	24.72 ± 0.69	24.77 ± 0.69
40	0.505	14.16 ± 0.89	1.59 ± 0.09	0.31 ± 0.07	1.28 ± 0.05	12.09 ± 0.76	12.11 ± 0.76
44	0.544	18.03 ± 0.74	n.m.	n.m.	1.21 ± 0.04	14.58 ± 0.60	14.62 ± 0.60
48	0.515	21.05 ± 1.19	2.09 ± 0.01	0.84 ± 0.04	1.25 ± 0.07	17.62 ± 0.99	17.66 ± 0.99
56	0.501	21.84 ± 1.37	1.55 ± 0.02	0.44 ± 0.06	1.11 ± 0.09	16.21 ± 1.02	16.25 ± 1.02
64	0.511	12.54 ± 0.94	1.46 ± 0.01	0.41 ± 0.02	1.06 ± 0.02	8.85 ± 0.66	8.88 ± 0.66
72	0.501	8.99 ± 0.87	1.63 ± 0.05	0.47 ± 0.03	1.16 ± 0.01	6.99 ± 0.68	7.01 ± 0.68
76	0.513	4.45 ± 0.37	n.m.	n.m.	1.40 ± 0.01	4.17 ± 0.35	4.18 ± 0.35
80	0.504	4.63 ± 0.55	1.63 ± 0.01	0.51 ± 0.03	1.12 ± 0.06	3.48 ± 0.41	3.49 ± 0.42
84	0.504	4.62 ± 0.31	n.m.	n.m.	1.36 ± 0.08	4.21 ± 0.28	4.23 ± 0.28
88	0.500	7.06 ± 0.64	1.66 ± 0.02	0.37 ± 0.03	1.28 ± 0.05	6.07 ± 0.55	6.09 ± 0.55
96	0.505	8.16 ± 0.69	1.70 ± 0.03	0.47 ± 0.05	1.22 ± 0.07	6.68 ± 0.57	6.71 ± 0.57
104	0.507	9.38 ± 0.78	1.75 ± 0.01	0.45 ± 0.03	1.30 ± 0.06	8.15 ± 0.68	8.18 ± 0.68
108	0.500	6.28 ± 0.37	n.m.	n.m.	1.37 ± 0.04	5.76 ± 0.34	5.79 ± 0.34
112	0.502	3.78 ± 0.44	1.83 ± 0.02	0.45 ± 0.03	1.38 ± 0.03	3.49 ± 0.41	3.51 ± 0.41
115	0.500	4.42 ± 0.29	n.m.	n.m.	1.30 ± 0.05	3.85 ± 0.25	3.86 ± 0.25
119	0.507	8.67 ± 0.80	1.63 ± 0.02	0.41 ± 0.02	1.22 ± 0.02	7.07 ± 0.66	7.10 ± 0.66
126	0.500	10.35 ± 0.75	1.58 ± 0.02	0.34 ± 0.04	1.24 ± 0.07	8.62 ± 0.62	8.65 ± 0.62
130	0.500	8.59 ± 0.89	1.51 ± 0.01	0.41 ± 0.06	1.10 ± 0.10	6.32 ± 0.65	6.35 ± 0.65
139	0.513	7.52 ± 0.78	1.53 ± 0.03	0.61 ± 0.03	0.92 ± 0.04	4.62 ± 0.48	4.64 ± 0.48
147	0.511	6.93 ± 0.73	1.46 ± 0.01	0.50 ± 0.04	0.96 ± 0.06	4.45 ± 0.47	4.47 ± 0.47
155	0.503	7.10 ± 0.68	1.36 ± 0.01	0.30 ± 0.02	1.07 ± 0.04	5.07 ± 0.49	5.10 ± 0.49
162	0.508	7.27 ± 0.73	1.32 ± 0.01	0.32 ± 0.04	1.00 ± 0.07	4.86 ± 0.49	4.89 ± 0.49
170	0.502	6.10 ± 0.66	1.33 ± 0.02	0.39 ± 0.07	0.94 ± 0.13	3.83 ± 0.41	3.86 ± 0.42
178	0.503	6.65 ± 0.68	1.21 ± 0.05	0.22 ± 0.09	0.98 ± 0.13	4.38 ± 0.45	4.41 ± 0.45
182	0.550	2.79 ± 0.25	n.m.	n.m.	0.95 ± 0.08	1.77 ± 0.16	1.78 ± 0.16
186	0.513	2.65 ± 0.46	1.33 ± 0.01	0.47 ± 0.03	0.85 ± 0.04	1.52 ± 0.26	1.53 ± 0.27
194	0.507	2.59 ± 1.29	1.35 ± 0.02	0.43 ± 0.05	0.92 ± 0.08	1.59 ± 0.79	1.60 ± 0.80
202	0.504	3.41 ± 0.48	1.24 ± 0.02	0.40 ± 0.02	0.84 ± 0.01	1.92 ± 0.27	1.94 ± 0.27
210	0.503	2.48 ± 0.51	1.38 ± 0.08	0.43 ± 0.09	0.95 ± 0.11	1.58 ± 0.32	1.60 ± 0.33
218	0.499	3.23 ± 0.72	1.22 ± 0.03	0.33 ± 0.06	0.89 ± 0.10	1.92 ± 0.43	1.94 ± 0.43

[a] All the ratios were calibrated using KN Standard Be 0152 with a $^{9}Be/^{10}Be$ ratio of 2.709×10^{-11} (Nishiizumi et al., 2007) and using a ^{10}Be half-life of 1.387×10^{6} years (Chmeleff et al., 2010; Korschinek et al., 2010).
[b] Total Be was measured using ICP-OES following the standard procedure.
[c] Amount of detrital Be was yielded subtracting mass of authigenic Be from total amount of Be.
[d] Authigenic amount of Be was measured using ICP-MS from sediments leached in weak acid (Bourles et al., 1989).
[e] The ratios are corrected for radiogenic decay based on the radiocarbon dating results of major sedimentary units from adjacent core records (Domack et al., 2005). As expected, nevertheless, there is little departure (<1%) from the un-corrected concentrations of authigenic ^{10}Be.
[f] n.m. means not measured.

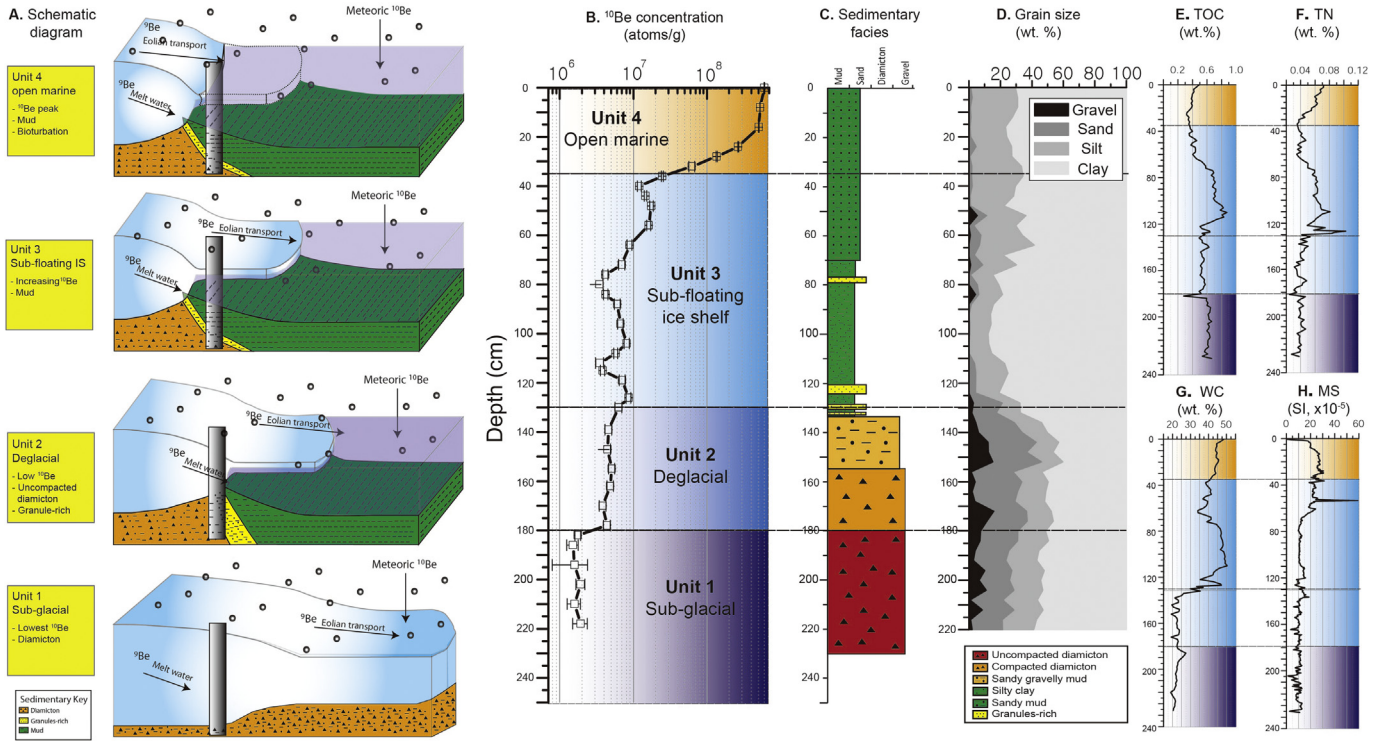

Fig. 3. Sequential reconstruction of LBIS retreat and results of core analysis. A: Schematic diagram of the LBIS showing the movement of beryllium isotopes and sedimentary facies with time. Meteoric ^{10}Be produced in the atmosphere falls out and is incorporated into the ocean but ^{9}Be originates mainly from bedrock. The area experienced four different depositional settings: Unit 1: Subglacial environment; Unit 2: deglacial environment; Unit 3: Sub-floating ice shelf environment; and Unit 4: Open marine environment. B: Variation in ^{10}Be concentration, which increases significantly under open marine conditions. C: Sedimentary facies logged on the basis of Domack et al. (2005) D: Grain size distribution of the core. E, F, G and H: Total organic content, total nitrogen, water content and magnetic susceptibility, respectively (Jeong et al., 2014).

^{9}Be concentration by the ^{10}Be/^{9}Be ratio measured by Accelerator Mass Spectrometry (AMS). We corrected ^{10}Be decay using several geochronological markers in the sediment cores: i) the age of the lowermost layer was assumed LGM based on sedimentary facies, ii) the age of the transition zone between grounded ice and floating ice shelf was estimated by comparison to Domack et al. (2005), and iii) the bottom of the uppermost layer was assumed to date to 2002. Between these markers, we assumed a constant sedimentation rate, then corrected the concentration as shown in Table 1. However, the difference between the uncorrected and corrected concentration is negligible due to the long half-life of ^{10}Be (1.387×10^{6} yr).

Beryllium-10 analyses were performed by 6 MV AMS at the Korea Institute of Science and Technology (KIST). The blank for the beryllium carrier averaged less than 6.5×10^{-15}. Authigenic ^{9}Be fraction samples were measured on the ICP-MS at Korea Basic Science Institute (KBSI) and the relative error of 1 standard deviation is <±2.5%. Total authigenic ^{9}Be fraction samples were measured on the ICP-AES at Center for Analytical and Life science Instruments in Korea University; the relative error of 1 standard deviation is <±6%.

3.2. Terrestrial in-situ ^{10}Be & ^{14}C exposure dating

To avoid the possibility of incomplete erosion under cold-based glacier (Sugden et al., 2005; Balco et al., 2013), we sampled glacial erratic cobbles, showing signs of exotic lithology (mostly granite and gneiss) and subglacial transportation such as polishing and smoothing on the corners. However, because of limited time available in the field, some samples were collected in low-lying areas rather than perched locations that would categorically exclude post-depositional relocation or burial by peri-glacial processes, and, as in other similar studies in Antarctica, it is not in general possible to exclude burial by frozen-based ice based on field criteria alone. Thus, to independently evaluate whether samples had experienced single periods of exposure at their present locations, we measured both in-situ ^{14}C and ^{10}Be on some samples. If the sample has experienced a single period of exposure since deglaciation, apparent exposure ages derived from ^{14}C and ^{10}Be concentrations will be equal. Periods of shielding or burial, that would cause the exposure age inferred from either nuclide to be incorrect, result in a difference between ^{14}C and ^{10}Be exposure ages. The degree of weathering and the site-specific conditions at each sample location were recorded. Topographic shielding was determined by measuring the inclination from each sample site to the top of surrounding mountain ridges and peaks (Table 2).

All samples for in-situ ^{10}Be and ^{14}C exposure dating were prepared at the Geochronology Laboratory at Korea University, Seoul, Korea. First, the samples were crushed and sieved, separated into 250–750 μm size fractions, and repeatedly etched in a dilute HF/HNO3 mixture following the standard method proposed by Kohl and Nishiizumi (1992). For analysis of ^{10}Be, we added ^{9}Be carrier with ^{10}Be/^{9}Be < 3.0×10^{-15}, then separated and purified Be by ion exchange chromatography and selective precipitation of BeOH at pH > 7. BeOH was oxidized by ignition in quartz crucibles at 800 °C for 10 min. BeO was mixed with Nb metal and loaded onto targets for measuring the ^{10}Be/^{9}Be ratio by accelerator mass spectrometry (AMS) at the AMS facility of Korea Institute of Science and Technology (KIST), Seoul, Korea. Isotope ratios were normalized to the ^{10}Be standards prepared by Nishiizumi et al. (2007). The measured isotope ratios were converted to cosmogenic ^{10}Be concentrations in quartz using the total ^{10}Be in the samples and the sample weights.

Table 2
Results of cosmogenic ^{10}Be surface exposure age of the erratics and bedrock on the Cape Marsh and Cape Framnes.

Sample	Latitude (°S)	Longitude (°W)	Elevation (masl)[a,b,c]	Thick-ness (cm)	Sample type & lithology	Shielding factor[d]	Quartz[e] (g)	Be Carrier[f] (g)	^{10}Be/^{9}Be (x 10^{-14}) [g, h]	^{10}Be Concentration (10^4 atoms g $^{-1}SiO_2$) [i,j]	Apparent age (kyr)[k]
R001	65.24525	59.44550	48	4.7	Erratic cobble, granite	0.99	20.1830	0.3818	4.76 ± 0.67	1.17 ± 0.10	2.01 ± 0.24
R002	65.24518	59.44527	48	4.5	Erratic cobble, granite	0.99	20.3185	0.4760	4.17 ± 0.76	0.61 ± 0.08	1.04 ± 0.16
R003	65.24561	59.44520	49	6	Erratic cobble, granite	0.99	14.5583	0.3920	5.52 ± 0.62	29.34 ± 1.07	5.06 ± 0.47
R004	65.24644	59.44457	46	5.5	Erratic cobble, granite	0.99	20.3301	0.3808	6.23 ± 0.46	28.47 ± 0.09	4.91 ± 0.45
R005	65.24646	59.44460	47	6	Erratic cobble, gneiss	0.99	20.8065	0.4084	4.28 ± 0.25	0.63 ± 0.26	1.10 ± 0.46
R006	65.24647	59.44466	47	3	Erratic cobble, gneiss	0.99	20.6888	0.3948	4.63 ± 0.31	1.03 ± 0.01	1.74 ± 0.15
F007	66.01637	60.56789	127	3.5	Erratic cobble, granodiorite	0.99	19.9561	0.3797	1.16 ± 0.10	9.14 ± 0.12	14.28 ± 1.26
F008	66.01593	60.56805	126	7.5	Erratic cobble, granodiorite	0.99	20.4397	0.3948	1.10 ± 0.68	8.55 ± 0.20	13.81 ± 1.25
F009	66.01477	60.55841	92	6	Erratic cobble, granodiorite	0.99	20.7645	0.3946	9.70 ± 0.57	6.93 ± 0.13	11.45 ± 1.02
F010	66.01466	60.55855	92	5.5	Erratic cobble, granodiorite	0.99	20.0896	0.3886	7.94 ± 0.46	4.96 ± 0.88	8.17 ± 0.72
F011	66.01478	60.55834	90	6.5	Erratic cobble, granodiorite	0.99	19.8757	0.3971	7.13 ± 0.66	4.14 ± 0.10	6.89 ± 0.62
F012	66.01477	60.55841	92	6	Erratic cobble, granodiorite	0.99	15.2570	0.4061	6.07 ± 0.74	3.78 ± 0.07	6.25 ± 0.55
F013	66.01447	60.55984	96	6	Erratic cobble, granodiorite	0.99	20.2940	0.3924	18.66 ± 1.26	17.68 ± 0.15	29.23 ± 2.5
F014	66.01549	60.56520	118	7	Erratic cobble, granodiorite	0.99	20.4078	0.4127	9.51 ± 0.64	7.14 ± 0.04	11.58 ± 1.01
F015	66.01542	60.56580	121	7	Erratic cobble, granodiorite	0.99	6.8660	0.3795	6.18 ± 3.09	8.23 ± 2.3	13.31 ± 4.02

[a]Elevation was calculated from atmospheric pressure which was measured using barometer from ground stations located by high-precision dGPS.
[b]Constant (time-invariant) local production rate (Lal, 1991; Stone, 2000). A value for sea level at high latitudes (4.5 atoms ^{10}Be g^{-1} quartz) was used.
[c]Constant (time-invariant) local production rate (Heisinger et al., 2002a, 2002b).
[d]Geometric shielding correction for topography was measured on an interval of 10°.
[e]Density of 2.65 g cm^{-3} was used based on the granitic composition of the surface samples.
[f] Low ratio (<3 × 10^{-15}) Be carrier having concentration of 1018.06 ppm was used.
[g]Isotope measurements were calibrated using KN Standard Be 0152 with a ^{9}Be/^{10}Be ratio of 8.558 × 10^{-12} (Nishiizumi et al., 2007) and using a^{10}Be half-life of 1.387 (±0.012) × 10^{6} years (Chmeleff et al., 2010; Korschinek et al., 2010).
[h]Uncertainties are reported at the 1σ confidence level.
[i]Propagated uncertainties include error in the blank, carrier mass (1%), and counting statistics.
[j]Propagated error in the model ages include a 6% uncertainty in the production rate of ^{10}Be and a 4% uncertainty in the ^{10}Be decay constant.
[k]Beryllium-10 model ages were calculated with the Cosmic-Ray Produced Nuclide Systematics (CRONUS) Earth online calculator version 2.2 (Balco et al., 2008).

Cosmogenic ^{10}Be concentrations were then converted to minimum surface-exposure ages using the online exposure age calculator of Balco et al. (2008; version 2.2), which utilizes the scaling method of Lal (1991) and Stone (2000), the default production rate calibration data set, and an assumed rock density of 2.65 g/cm^3.

Eleven samples whose ^{10}Be concentration was measured were additionally analyzed for quantifying in-situ ^{14}C (Table 3). Sample extraction was performed at Korea University following the method (Kim et al., 2016) modified from the previous ones (Lifton et al., 2001; Naysmith, 2007; Hippe et al., 2009; Pigati et al.,

Table 3
Results of in-situ produced cosmogenic ^{14}C. All the errors are 1σ.

Sample	Lab ID	Quartz (g)	$\delta^{13}C_{meas}$[a]	F[b]	CO_2 yield (μL)[c]	Dead $CO_{2(mL)}$[d]	^{14}C (10^4 atoms g^{-1})	^{14}C/^{10}Be
R001	KU140513	4.965	−32.4909	0.0176	324.9	1.5812	3.66 ± 0.18[e]	3.11 ± 0.16
R004	KU14705	4.997	−39.1828	0.0335	90.9	1.5857	7.24 ± 0.21[f]	2.54 ± 0.08
R006	KU140514	4.724	−31.3634	0.0155	374.0	1.4792	0.61 ± 0.04[e]	0.60 ± 0.04
F008	KU14706	4.959	−37.7469	0.0496	106.11	1.2307	13.70 ± 0.46[f]	1.60 ± 0.05
F009	KU14707	5.054	−38.3343	0.0413	76.44	1.3816	9.61 ± 0.51[f]	1.39 ± 0.07
F010	KU14708	3.495	−38.5917	0.0365	78.14	1.3996	8.27 ± 0.63[f]	1.67 ± 0.13
F013	KU140515	4.401	−33.0164	0.0290	391.4	1.4182	17.16 ± 0.65[e]	1.00 ± 0.04
F014	KU140516	4.612	−33.8506	0.0272	438.0	1.3898	14.92 ± 0.44[e]	2.09 ± 0.06

All the processes for calculating ^{14}C atoms in-situ produced in quartz are based on the equations employed in Donahue et al. (1990) and Naysmith (2007).
[a] Used for calibration with NIST oxalic acid (^{14}C/^{12}C: 134pMC) $\delta^{13}C = -17.8‰$).
[b] Calculation of fraction modern corrected for background (dead CO_2) with average (n = 6) value of 0.0012. Uncertainty causing from pressure gauge is 2.3 μg.
[c] Total CO_2 extracted from quartz with step-wise collection and purification.
[d] Low ratio (<3 × 10^{-15}) of background carrier spiked.
[e] Corrected for process blank with a mean ^{14}C concentration of 8.76 (±0.10) x 10^5.
[f] Corrected for process blank with a mean ^{14}C concentration of 1.49 (±0.11) x 10.

2010). ~ 5 g of clean quartz was loaded on the melting flux ($LiBO_2$) on the alumina (Al_2O_3) boat which was premelted in high vacuum state before the quartz was loaded and then was preheated with step-wise increase of temperature, from at 500 °C for 1.5 h and at 750 °C for 1.5 h for removing atmospheric ^{14}C contamination. In-situ ^{14}C in quartz was degassed and oxidized at 1100 °C for 3 h with an Ultra-High-Purity O_2 followed by subsequent cleaning steps with secondary oxidation in quartz-bead combustion furnace and cryogenic coil trap. The purified CO_2 was graphited, targeted and measured by 6 MV AMS facility installed at KIST. All the measured ratios were normalized and converted into ^{14}C concentration after subtracting processing blanks ($5.32 \pm 0.31 \times 10^5$ ^{14}C atoms). Our mean value for 4 aliquots of PP-4 (Cronus-R) is $3.37 \pm 1.78 \times 10^5$ ^{14}C atoms. The error ranges for the ^{10}Be and ^{14}C exposure ages in this study are shown as one standard deviation ($\pm 1\sigma$) and account for external uncertainties.

4. Results

4.1. Meteoric ^{10}Be variation from Larsen B embayment

Core EAP13-GC17 (Fig. 1) contains a sequence that includes a basal diamicton, an overlying granule facies in the middle section, and a mud facies at the top. The core can be classified into subglacial, deglacial, sub-floating ice shelf environment, and open marine environment on the basis of sedimentological characteristics (Domack et al., 1999, 2005) and the pattern and absolute concentration of meteoric ^{10}Be (Scherer et al., 1998) (Fig. 3). Meteoric ^{10}Be concentration increases steadily upwards within the uppermost (0–35 cm) section of the core (Fig. 3 and Table 1). We interpret this increase to reflect the increased accessibility of the site to meteoric ^{10}Be deposition as the edge of the ice shelf retreated toward the site: lowest concentrations reflect a subglacial environment, intermediate concentrations reflect a sub-ice-shelf environment where ^{10}Be deposition at the site is limited by sediment transport into the sub-ice-shelf cavity, and higher concentrations record an open-marine environment. Core top ^{10}Be concentrations reach 5.99×10^8 atoms g^{-1} sediment^{-1}, which is similar to values reported from open marine conditions that range from 5×10^8 to 5×10^9 atoms g^{-1} (Scherer et al., 1998; Sjunneskog et al., 2007). The observation that concentrations characteristic of open-marine conditions occur only in the uppermost part of the core implies that the LBIS was intact throughout the Holocene.

We could not find materials for conventional ^{14}C dating in the basal diamicton of our core, which is common in ice-proximal Antarctic marine environments that are extremely unfavorable for preservation of dateable organic material. Thus, we assume that the timing of the initiation of ice retreat is approximated by the radiocarbon ages reported by Domack et al. (2005) and Rebesco et al. (2014) for other cores recovered from the LBIS. Considering the similar sedimentological trends and geographical proximity of our coring site to other researchers' sites, the reported age (9.7–9.3 kyr BP) is likely to closely approximate the deglaciation age at our core site.

4.1.1. Unit 1: Subglacial facies (236-180 cm)

The lowest section of the core includes dark greenish gray, muddy, structureless and compacted diamicton (236-180 cm) with the water content ranged 19–27% (Fig. 3; Jeong et al., 2014). We interpret unit 1 to have been deposited underneath grounded glacier-ice and attribute the low water content to dewatering and compaction due to the high overburden pressure or basal freeze-on of the ice sheet (Evans et al., 2005) (Fig. 3). The ^{10}Be concentration ranges from 1.5×10^6 to 1.9×10^6 atoms g^{-1} in this section (Table 1). Underneath a grounded ice sheet, direct atmospheric input of ^{10}Be to sediment is not possible, so the only potential sources of meteoric ^{10}Be are (i) basal melting of glacier ice with extremely low ^{10}Be concentrations (order 10^4 atoms g^{-1}; see Beer et al., 1988) or (ii) residual ^{10}Be in sediment that may have been deposited under open-marine conditions in a previous interglacial period, but not subsequently removed by glacial erosion (Scherer et al., 1998). The concentration we observe in Unit 1 is similar to background levels of ^{10}Be concentration in Ross Sea subglacial sediment reported by Scherer et al. (1998), which is consistent with our interpretation of Unit 1 as a subglacial deposit.

4.1.2. Unit 2: Deglacial facies (180-129 cm)

Unit 2 includes three sub-facies; (1) greenish gray muddy, uncompact diamicton (180-155 cm), (2) dark greenish gray, crudely stratified granule rich-sandy gravely mud (155-134 cm), and (3) light olive gray, interbedded silty clay and granulated, sandy silt-clay aggregates (134-129 cm) (Fig. 3). This unit fines upward and also increases in water content, which is consistent with deposition in a near-grounding zone between ice sheet and ice shelf (Powell et al., 1996; Domack et al., 1999; Evans and Pudsey, 2002; Evans et al., 2005) (Fig. 3). Subglacial water discharge near the grounding zone is expected to cause grain-size sorting, and in this environment basal diamicton is commonly overlain by stratified granular facies (Domack et al., 1999). Furthermore, observed sorting and stratification might be derived from the mechanisms of melt water or tidal pumping (Domack and Williams, 1990; Anandakrishnan and Alley, 1997; Domack et al., 1999; Evans et al., 2005). The range of ^{10}Be concentration in the unit 2 is between 3.8×10^6 and 6.3×10^6 atoms g^{-1} (Table 1). We interpret the concentration of ^{10}Be in unit 2 that is higher than in unit 1, but lower than expected for open-marine conditions, to reflect grounding line retreat that allowed access of marine waters and sediment to the site, but continued cover by an extensive ice shelf limiting transport of atmospherically-derived ^{10}Be into the sub-ice-shelf cavity and to the core site (Fig. 3).

We estimate the age of this unit from radiocarbon dating of nearby cores which has very similar sedimentary facies. Domack et al. (2005) investigated diatoms from six marine sediment cores in LBIS area and acquired uncorrected ^{14}C deglaciation age 10,600 and 9210 yr, which is consistent with other sites throughout the NEAP and most likely reflects deglaciation during the early-Holocene climatic optimum (EHCO: 11–9.5 kyr) (Pudsey et al., 2006; Bentley et al., 2009; and references therein). Compared to other cores in the LBE described by Domack et al. however, our core site had a higher sedimentation rate during sub-floating ice shelf condition (unit 3). This is most likely related to variations in the pattern of ice flow (Fig. 1), but further study would be required to understand this in detail.

4.1.3. Unit 3: Sub-floating ice shelf facies (129-35 cm)

The composition of unit 3 is (1) light olive gray homogeneous silty clay (129-70 cm) and (2) light olive gray to moderate olive brown, slightly bioturbated, laminated sandy mud (70-35 cm). The boundary between unit 2 and unit 3 is well recognized due to the rapid upward-fining facies (Fig. 3). Within unit 3, sharp contacts were observed at two layers (121–123 cm and 80 cm) (Fig. 3), that were substantially coarser than muddy sediment that dominates this unit. The muddy facies are the most abundant in unit 3, and are characteristic of a distal sub-ice shelf environment or open marine conditions (Domack et al., 1999; Evans and Pudsey, 2002; Evans et al., 2005). In general, there are two potential sediment sources for coarser grains in sub-floating ice shelf environments: the grounding zone at the ice-proximal end of the ice shelf, and the vicinity of the calving margin at the distal end of the ice shelf. A null zone between these two margins has limited coarse sediment

input. Therefore, the facies succession fines upward from grounding zone to null zone, and then as ice retreat is proceeding, coarsens upward with an increase in ice-rafted debris derived from the calving margin (Michalchuk et al., 2009). Based on the model of Domack et al. (1999), we interpret the environments of unit 3 as follows: i) glacial marine muds proximal to the grounding zone (129-112 cm), ii) null zone (112-80 cm), and iii) around the calving line (80-35 cm). In addition, well-developed thin laminations identified by radiography from 61 to 35 cm also indicates that this sub-unit still occupied the sub-floating ice shelf environment although it may have been relatively closer to the calving line (Domack et al., 1999). ^{10}Be concentrations in this unit are between 3.5×10^6 and 2.5×10^7 atoms g^{-1} (Table 1). In the lower section (129-79 cm) of unit 3, the ^{10}Be concentration is relatively constant, but increases by nearly an order of magnitude in the upper section (79-35 cm) with the change from a near-grounding-zone environment to a distal sub-ice shelf environment (Table 1). Still, the highest concentration in this unit is nearly an order of magnitude below that indicative of an open marine environment (5×10^8 atoms g^{-1} to 5×10^9 atoms g^{-1}; see Arnold, 1956; Goel et al., 1957; Merrill et al., 1960). Consequently, this shows that the LBIS remained in place during the mid-Holocene climate optimum (MHCO).

4.1.4. Unit 4: Open marine facies (35-0 cm)

Unit 4 is characterized by extinction of the thin lamination succession and the emergence of bioturbation which is very similar to sedimentary facies deposited in an open marine environment. Likewise, the ^{10}Be concentration in this unit ranges from 6.2×10^7 atoms g^{-1} to 6.0×10^8 atoms g^{-1}, which is similar to ^{10}Be concentrations in open marine environments elsewhere as discussed above (Arnold, 1956; Goel et al., 1957; Merrill et al., 1960), which is also supported by rapid increase in productivity (Fig. 4F; Jeong et al., 2014). We attribute the onset of open marine conditions recorded by Unit 4 to the LBIS collapse in 2002. Alternatively, given the relatively high depositional rate, the initial interval of Unit 4 at 35-20 cm is more likely a product of a shift in sub-shelf ocean circulation and increased sediment advection due to nearness to retreating calving margin (White et al., 2016), limiting only the top 20 cm deposit to open marine. The observation that ^{10}Be concentrations reach open-marine levels only once in the core shows that only a single collapse of the LBIS took place at this site, and agrees with a similar conclusion based on diatom valve abundance in the nearby core NBP01-07 KC3 (Domack et al., 2005).

4.2. In-situ ^{10}Be & ^{14}C exposure ages of terrestrial erratics

We recovered six metamorphic erratic clasts (R001-R006; Table 2) from Cape Marsh, an ice-free area bounded by steep cliffs on the southern margin of Robertson Island, located between the LAIS and LBIS (Fig. 4). These erratics occur nearly 50 m above sea level (a.s.l.). Apparent ^{10}Be exposure ages of these erratics fall into two age groups of 5 ka and 2-1 ka (Table 2 and Fig. 5). We measured both ^{14}C and ^{10}Be in three samples, of which two had concordant ^{14}C and ^{10}Be concentrations, indicating that they experienced a single period of exposure since emplacement due to ice retreat (Fig. 6). The ^{14}C concentration of a third (R006) one was significantly lower than would be expected from the ^{10}Be concentration, indicating that exposure of this sample was interrupted by a period of burial. The minimum possible total duration of exposure and burial for this sample is 16.3 ka, suggesting that this boulder may have been incorporated from an older deposit. Overall, consideration of either all data or only the two samples with concordant ^{14}C and ^{10}Be concentrations indicates ice retreat from this site between 5 and 2 ka for the northern sector of the LBE. It is not clear from these data whether the spread of ages is best explained by slow thinning of the regional ice shelf, or by thinning of the ice shelf near 5 ka followed by instability of some surface boulders or slow retreat of the small, locally derived ice cap on Cape Marsh itself. Given more extensive paleo ice cover, however, we cannot rule out the possibility of a supraglacial debris field (or moraine) that began accumulating by 5 ka and was lowered to the ice surface by 2 ka.

Cape Framnes, located on the northeastern margin of Jason Peninsula (Fig. 4), hosts ice-free areas strewn with frost-shattered

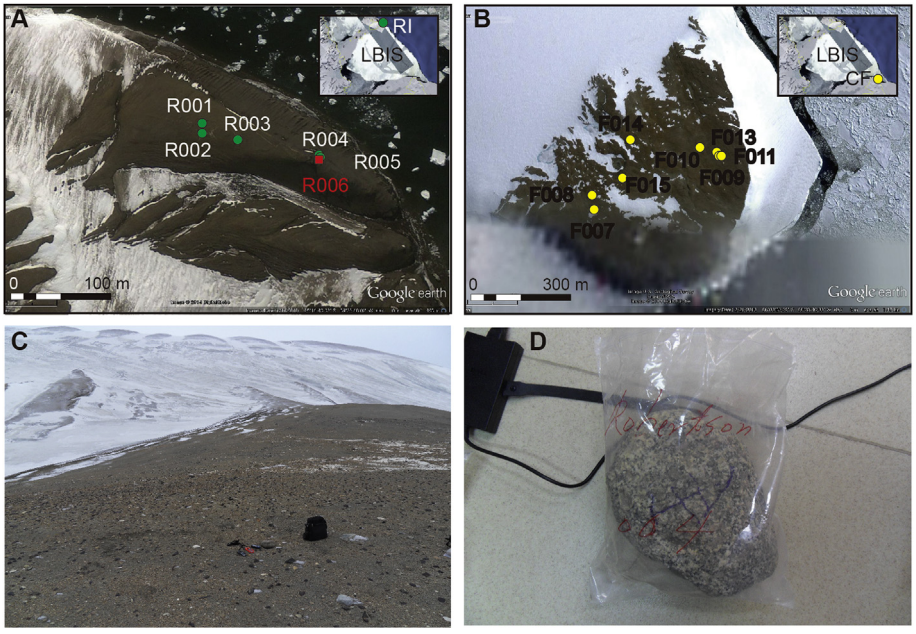

Fig. 4. Sampling locations for in situ ^{10}Be exposure dating. We collected erratic boulders from Robertson Island and Cape Framnes contiguous to LBIS. A: Roberston Island (RI). B: Cape Framnes (CF). (C) Surface exposed by retreating glacier from which erratics were collected at RI. (D) Close-up view of granite erratic boulder (R004) in (C) contrasted with local meta-sedimentary angular detritus.

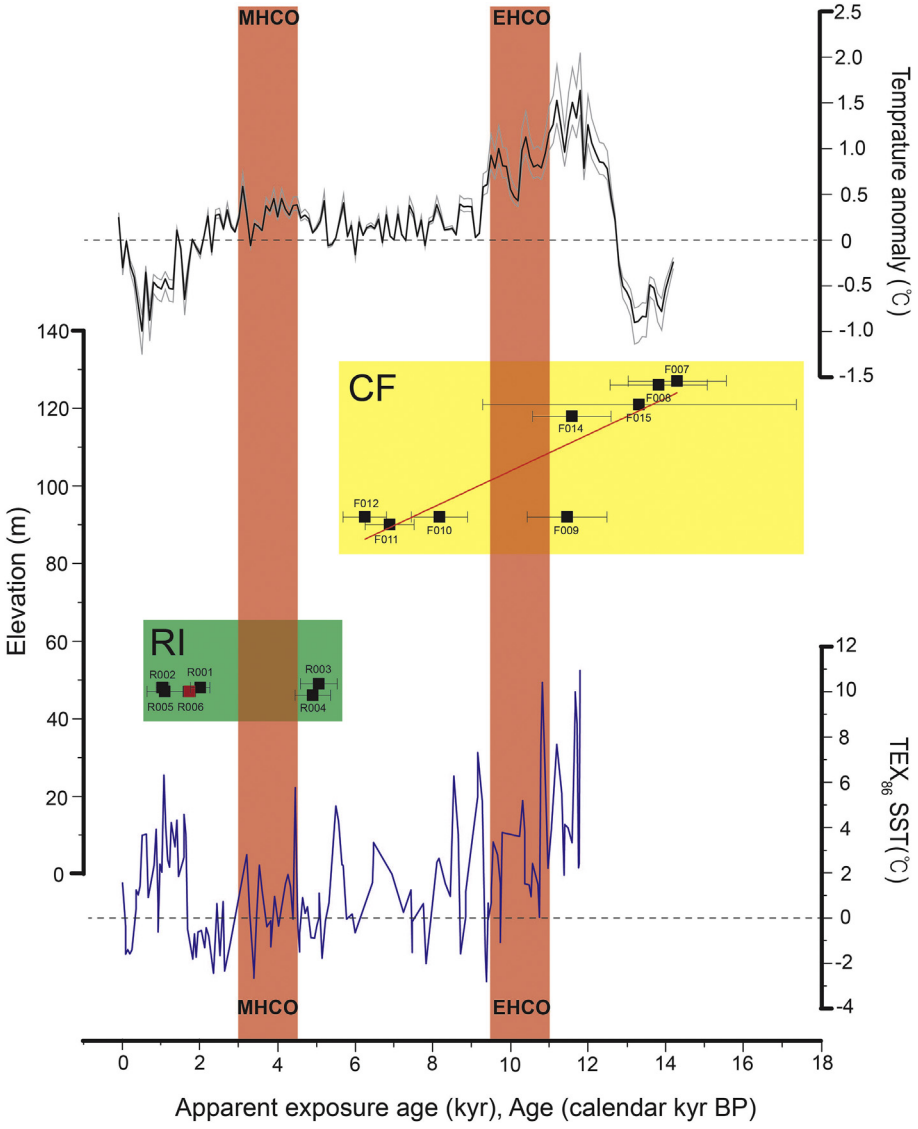

Fig. 5. Apparent ^{10}Be ages with elevation from the Cape Marsh in Robertson Island and Cape Framnes. Error bars show 1σ external uncertainties. Temperature anomaly indicates 100-yr averaged ice-core temperature reconstructed from James Ross Island (57° 41.10′ W, 64° 12.10′ S), relative to the 1961–1990 mean conducted by Mulvaney et al. (2012) (black line; the gray lines indicate the standard error of the calibration dependence). TEX_{86} SST is sea surface temperature (SST) converted from the values of tetraether index of tetraethers with 86 carbon atoms (TEX_{86}) from sediment core at ODP Site 1098 (1098B: 64° 51.162′ S, 64° 12.4795′ W, 1010 m water depth) with a modified calibration of Shevenell et al. (2011) (blue line). Vertical colored bands indicate mid-Holocene and Early-Holocene climate optimum in the NEAP (northeast Antarctic Peninsula) region. (For interpretation of the references to color in this figure legend, the reader is referred to the Web version of this article.)

bedrock outcrops (felsenmeer). Bedrock displays NW-SE striations and is overlain by erratic clasts. Other evidence of past glacial erosion on these ice-free areas includes deeply scoured hollows that host several lakes as well as dry lakes with polygonal patterned ground. In addition, several moraine ridges are present, which we interpret as lateral moraines deposited at the margin of an ice shelf in contact with the land surface (Fig. 7). At heights between 118 and 127 m a.s.l., four erratic boulders have apparent exposure ages of 14–12 ka (F007, F008, F014, F015; Table 2). At around 90 m a.s.l., four erratic boulders have apparent exposure ages of 8–6 ka and 11 ka (F009, F010, F011, F012; Table 2). We measured both ^{14}C and ^{10}Be in five boulders from this site and all displayed concordant ^{14}C and ^{10}Be concentrations, indicating that they experienced a single period of uninterrupted exposure. However, one boulder (F013) displays concordant ^{14}C and ^{10}Be concentrations, but an apparent exposure age of 29 ka. Although this age well predates the LGM, the ^{14}C-^{10}Be concordance requires uninterrupted exposure and excludes a scenario in which this sample was exposed at this site prior to the LGM, buried by ice at the LGM, and then re-exposed during deglaciation between 8 and 14 ka, unless the period of LGM ice cover was extremely short, in this case less than ca 1-2 ka. A more likely explanation may be that this sample was derived from rockfall onto the glacier surface rather than subglacial quarrying, so was exposed at the surface for a long time before it arrived at its present location. In any case, we interpret these results to indicate that Cape Framnes was exposed by ice sheet or ice shelf thinning between 14 ka and 8 ka.

5. Discussion

5.1. Spatial difference in ice thinning in the Larsen B and adjacent area

The different apparent exposure ages between Cape Marsh and

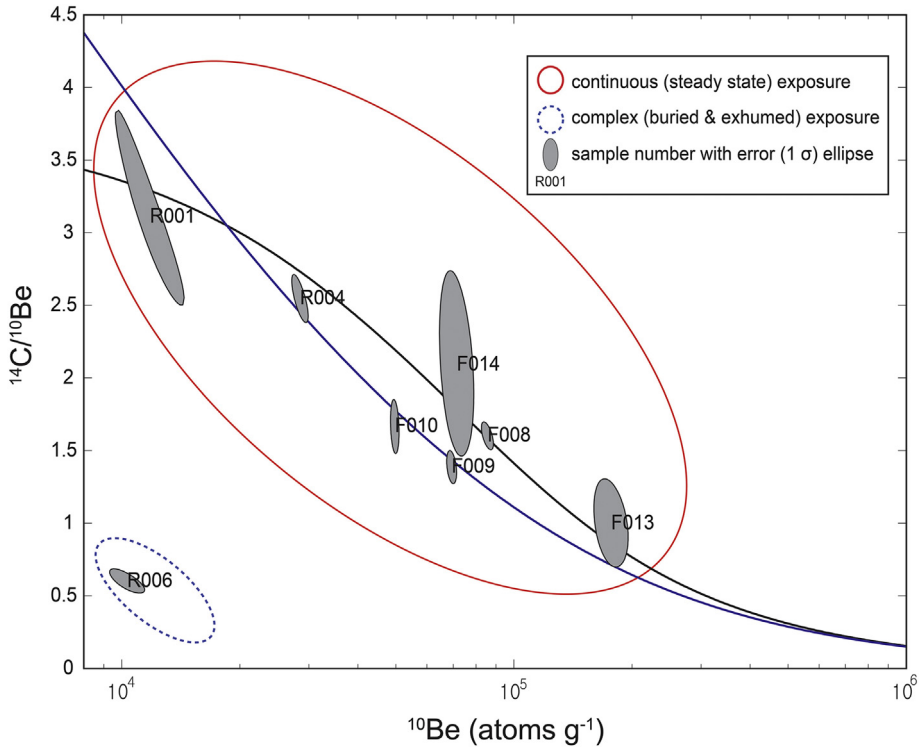

Fig. 6. Evaluation of the likelihood of continuous exposure of the erratics using the $^{14}C/^{10}Be$ ratio versus ^{10}Be concentration for unit nuclide production rates (14.45 at g^{-1} quartz^{-1} for ^{14}C and 4.5 at g^{-1} quartz^{-1} for ^{10}Be). Uncertainty ellipses indicate 1σ external uncertainties.

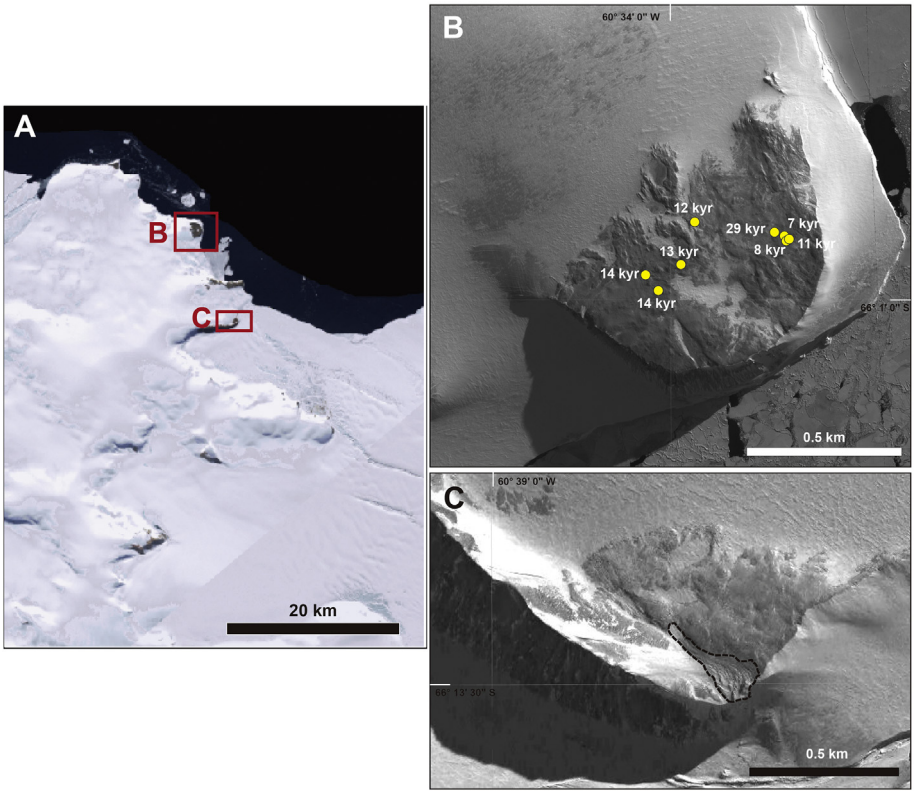

Fig. 7. A: The tip of the Jason Peninsula and boundary between LBIS and LCIS. It shows outcrop sites where we took samples for in situ ^{10}Be and ^{14}C measurement and lateral moraine was observed through satellite image. B: Sampling site at Cape Framnes. Yellow circles show each sample locations. Geomorphic features related with glacier including striations, lake and dry lake were observed in field. C: A group of looped lateral moraines are observed, which was likely to be formed during the historic or recent glacial advances. The image of A is from USGS Landsat Image Mosaic of Antarctica. The satellite imagery of (a) and (b) is modified from a map compiled by Spences Niebuhr, Polar Geospatial Center (http://www.pgc.umn.edu/imagery/aerial/antarctica). (For interpretation of the references to color in this figure legend, the reader is referred to the Web version of this article.)

Cape Framnes combined with meteoric ^{10}Be analysis of the marine sediment core allows for the comparison of deglacial history between the northern and southern LBE. Based on our exposure ages discussed above and other evidence for ice shelf change in this region, we suggest the glaciers of Cape Marsh located between LAE and LBE experienced the following history: i) complete deglaciation of the currently ice-free areas at 1.0–5.1 ka, ii) grounding line advance, glacier thickening, and expansion of frozen-based ice over our sampling sites during the late Holocene, most likely after 1.0 ka as suggested by the timing of late Holocene ice shelf formation in the LAE (Brachfeld et al., 2003), and iii) complete re-exposure of these sites after recent ice shelf breakup and lowering of the glacier surface (Fig. 8). In contrast, exposure ages from Cape Framnes show that the SLBE experienced significant deglaciation (i.e. ice thinning by up to 40 m) until ~6-8 ka but thereafter remained more stable than the northern LBE.

Recently reported paleo-ice flow directions of the NEAP ice sheet based upon new seabed imagery (Lavoie et al., 2014) may provide an opportunity to reconstruct deglaciation and changes in ice configuration across the LBE during the late Quaternary. At the LGM, the Antarctic Peninsula Ice Sheet extended to the middle–outer shelf and included several ice domes and troughs in the northeastern sector of the Antarctic Peninsula (Figs. 1 and 8; Lavoie et al., 2014). Glacial ice in the NLBE flowed northeast along the Robertson Trough between Robertson Dome and Hektoria Dome. Ice in the SLBE flowed southeast and merged into the Jason Trough, which is consistent with NNE-SSW striations on bedrock at Cape Framnes (Lavoie et al., 2014). The difference in exposure ages for deglaciation between Cape Marsh and Cape Framnes may reflect the separation of ice flow due to ice domes present at the LGM. Although there is no evidence for deglaciation at Robertson Island until about 5 ka, our exposure ages suggest the transition from ice dome to ice cap, or separation of the Robertson Island ice cap from the Robertson Dome, initiated no later than about 5 ka and may have continued until 2–1 ka. The ice shelf near Robertson Island then re-advanced, resulting in the pre-1997 configuration (Fig. 8). The timing and pattern of ice retreat in the NLBE is consistent with that from the LAIS (Brachfeld et al., 2003; Balco et al., 2013).

Alternatively, exposure ages from Cape Marsh may record collapse of Robertson Dome between 5 and 2 ka (Fig. 8), which is broadly coincident with the marine (Brachfeld et al., 2003) and terrestrial (Balco et al., 2013) records for the period 3.8–1.7 ka in the LAIS. Likewise, exposure ages from Cape Frames may record surface lowering at Hektoria Dome and LCIS between 14 and 6 ka ago. The profile of meteoric ^{10}Be concentration indicates that an ice shelf was present at the core site throughout the Holocene, implying that the recent collapse was unprecedented in the very position of LBIS (Fig. 3). If grounded ice at Hektoria Dome persisted until 6 ka, it may have contributed to stability of the LCIS during mid-Holocene warming by obstructing water circulation to the inner shelf.

5.2. Regional paleoclimate comparison with other ice shelves in northeastern AP

Our new exposure ages for deglaciation at Cape Framnes indicate that initial ice retreat and thinning in the LBE and possibly northern LCE commenced at ~14 ka, which is consistent with the timing of ice retreat in most areas in AP (14-13 ka) (Heroy and Anderson, 2005; Evans et al., 2005), and continued through the early Holocene (Bentley et al., 2009). Along much of the NEAP margin grounded ice and ice shelves are likely to have reached its modern configuration by 9.5–11 ka (Bentley et al., 2009; Johnson et al., 2011; Ó Cofaigh et al., 2014). The transition from grounded ice to ice shelf occurred between 10.7 and 10.9 ka in PGC (Pudsey and Evans, 2001; Pudsey et al., 2006), and it appears that the timing of the transition at the LAE and LBE was similar. This transition was completed by 10.7 ± 0.5 ka at the inner LAIS (Brachfeld et al., 2003), and 10.6 ± 0.1 ka at the inner LBIS (Domack et al., 2005).

Terrestrial exposure ages from the LAE suggest that very thick ice was at least 470 m above present sea level during the EHCO (Balco et al., 2013) (Fig. 9). After the EHCO, our exposure ages indicate that deglaciation was ongoing, but possibly at a slower rate than during the mid-Holocene climate optimum (MHCO). Exposure ages at Cape Framnes indicate 40 m of ice surface lowering between 14 ka to 6 ka, spanning the EHCO, in the SLBE. On the other hand, 80 m of ice thinning between 4.8 and 3.4 ka took place at PGC during the MHCO (Balco et al., 2013) (Fig. 9). This difference is not obviously consistent with temperature reconstructions showing a warmer EHCO, but the significance of this is not clear because local thinning rates may reflect local ice sheet geometry or proximity to the grounding line rather than regional mass balance. After the EHCO, our chronology suggests that regional ice sheet and/or ice shelf thinning proceeded from north to south, which may be related to the north-south variation in the stability of ice shelves observed in the Holocene. Ice-free areas appeared 6.5–7.5 ka near PGC, 4.7–6.2 ka in the LAE (Balco et al., 2013) and 4.9–5.1 in the NLBE (this study) (Fig. 9). Likewise, both onshore and offshore data shows a sequence of deglaciation from North to South: PGC was ice-free at 3.4–4.8 ka with ice shelf collapse at 2-5 ka, the LAIS was absent at 1.4–3.8 ka, and NLBE glaciers may have retreated at 1.0–2.0 ka (Fig. 9). Overall, these observations are consistent with the hypothesis that more northerly parts of the Larsen ice shelf system are more sensitive to climatic or oceanic warming.

Several hypotheses have been suggested to explain why the LBIS was more stable than other nearby ice shelves during the Holocene. Domack et al. (2005) suggested that the ice shelf thickness was the important factor, such that a thicker ice shelf is less susceptible to basal melting. However, available evidence is not sufficient to determine whether or not the LBIS was anomalously thick (Hodgson et al., 2006). Alternatively, Hodgson et al. (2006) suggested that early-Holocene deglaciation in the northern AP may have facilitated access of warmer ocean waters to more northerly ice shelves. However, our exposure ages at Cape Framnes indicate early-Holocene deglaciation in the southern LBE, which is not consistent with this hypothesis. Instead, we propose that asynchronous deglaciation between onshore and offshore data at more southerly sites (Fig. 9) is explained by the existence of topographic obstacles that physically interrupt approach of warmer ocean water. One possibility is that remnant grounded ice of Robertson and Hektoria domes (Lavoie et al., 2014) may obstruct circulation of warmer ocean water (Fig. 8). According to the calculation of ice dome thickness by Lavoie et al. (2014), Hektoria dome was 1150–1375 m thick, and Robertson dome was 800–1200 m thick at the LGM. Slow ice sheet thinning at Cape Framnes in the early Holocene (40 m thinning from 14 ka to 6 ka) may indicate that the ice domes were still present in part during the early Holocene. Therefore, we propose that local topography and ice sheet configuration, rather than ice shelf thickness or the timing of deglaciation, may be responsible for the greater Holocene stability of the LBIS in relation to other nearby ice shelves.

6. Conclusion

We have applied a record of meteoric ^{10}Be variation in marine sediments in the LBE and in situ ^{10}Be exposure ages from the margins of LBE to reconstruct deglacial history across the LBE during the late Quaternary. Our data document spatio-temporal differences in post-LGM ice change across the LBE. Ice thinning in

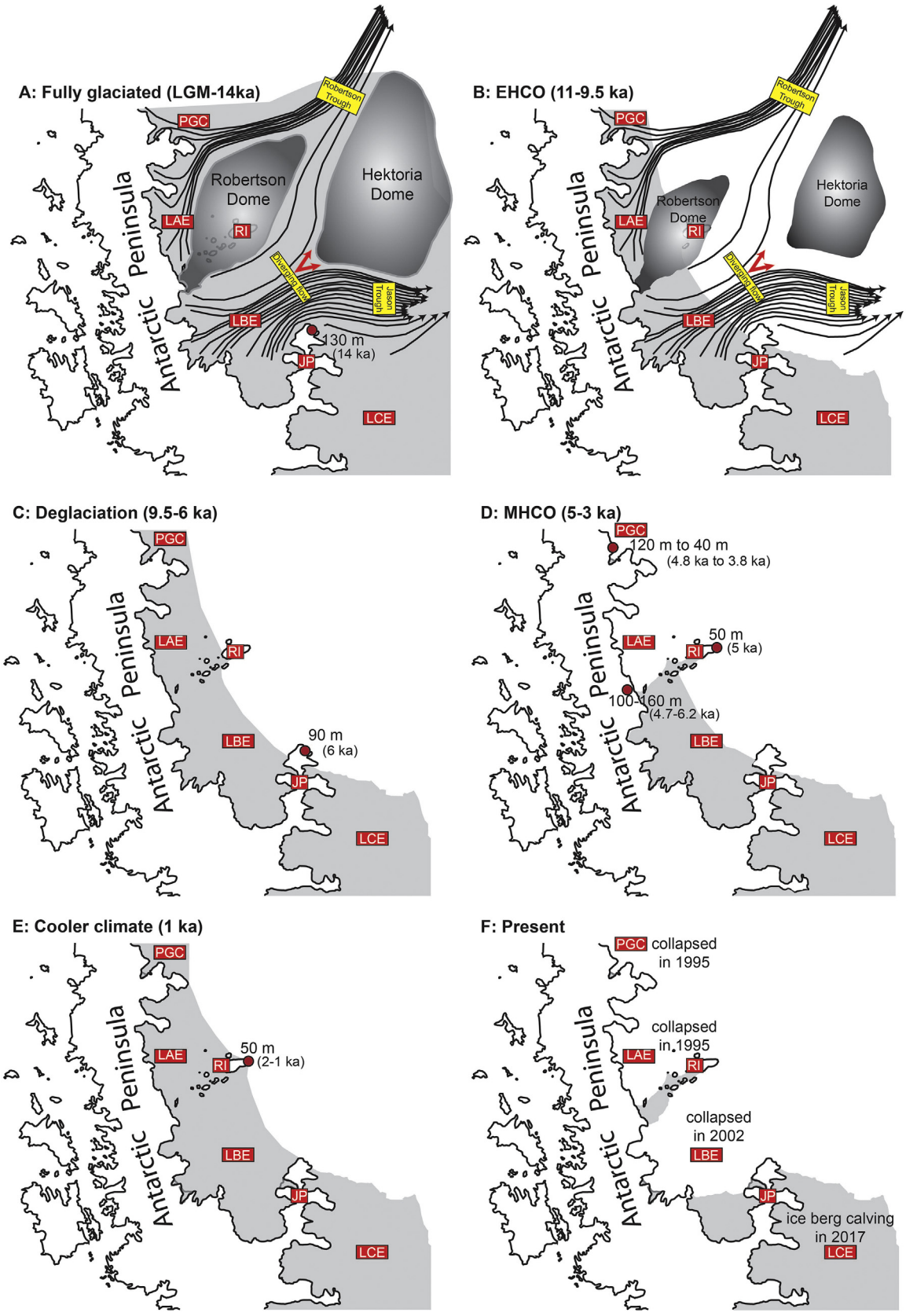

Fig. 8. A cartoon showing ice configuration in NEAP based on a seafloor map (Lavoie et al., 2014) and other studies (Balco et al., 2013; more references in there). Red filled circles on the maps indicate paleo ice thickness that is difference to present above present sea level derived from cosmogenic exposure ages (Balco et al., 2013; this study). Abbreviation: EHCO, early Holocene climate optimum; MHCO, middle Holocene climate optimum. (For interpretation of the references to color in this figure legend, the reader is referred to the Web version of this article.)

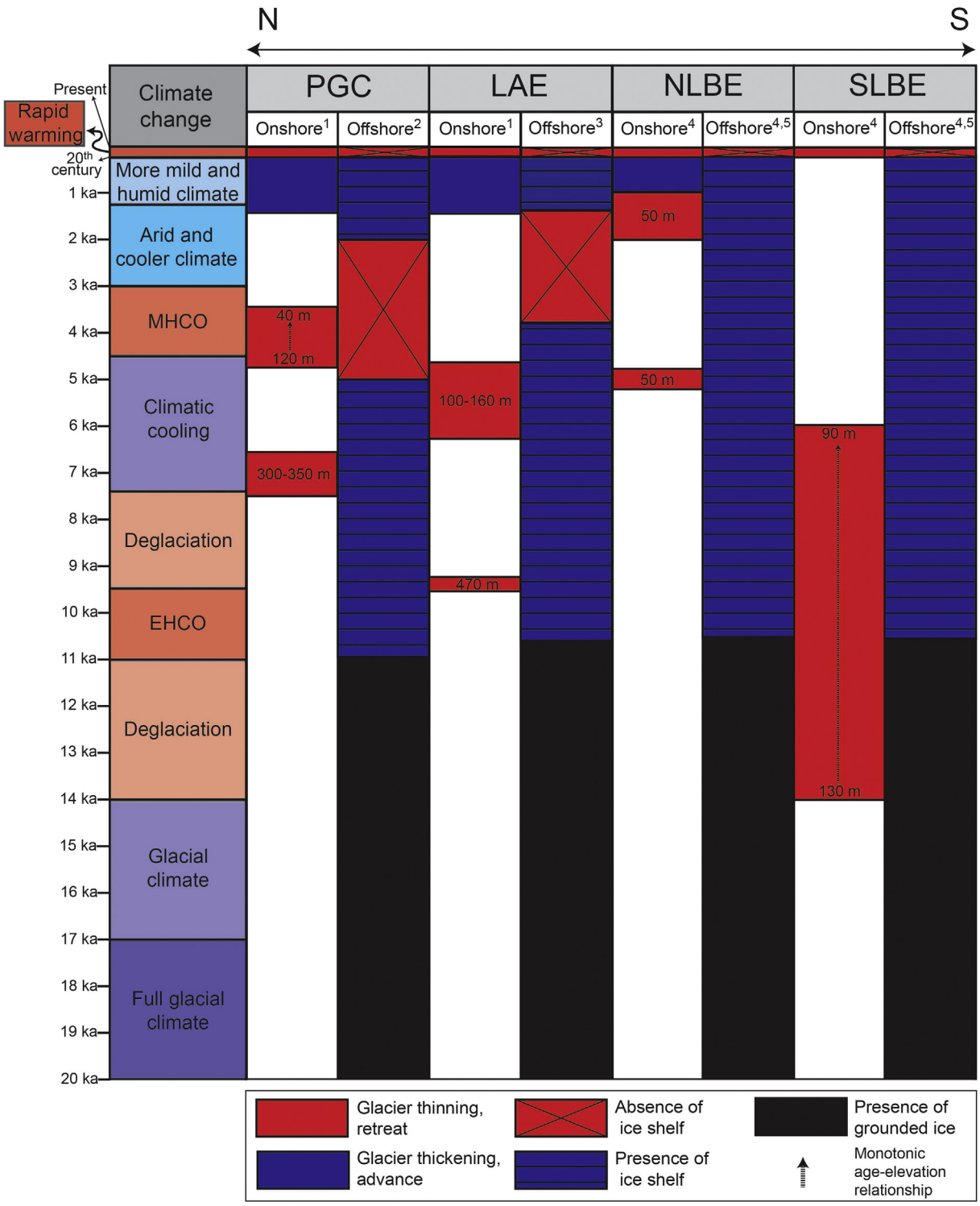

Fig. 9. Comparison of a climate synthesis modified from Ingólfsson et al. (2003) with relative timing records of deglacial events from five geographic locations listed from southernmost to northernmost part in the northeast Antarctic Peninsula region. Elevation of ice surface constrained by cosmogenic exposure dating is given in red columns labelled. Dashed arrow in columns indicate monotonic age-elevation relationship which can help us estimate approximate local ice thinning rate at the site. Abbreviations are PGC, Prince Gustav Channel; LAE, Larsen A embayment; NLBE, northern Larsen B embayment; SLBE, southern Larsen B embayment; EHCO, early Holocene climate optimum; MHCO, middle Holocene climate optimum. References: 1, Balco et al. (2013); 2, Pudsey and Evans (2001); 3, Brachfeld et al. (2003); 4, this study; 5, Domack et al. (2005). (For interpretation of the references to color in this figure legend, the reader is referred to the Web version of this article.)

the SLBE started no later than 14 ka and lasted until 6 ka, then remained relatively limited from 6 ka to its latest collapse. In contrast, the NLBE likely reorganized after a complete collapse during the late-Holocene, which is similar to the history of the LAIS immediately to the north. We use these data to reconstruct a regional pattern of deglaciation history along the northeastern Antarctic Peninsula (NEAP). The NEAP had a southward delayed response to atmospheric warming since the mid-Holocene, and we

suggest that this was the result of local topography, bathymetry, and ice sheet configuration, rather than differences in regional climate forcing or some properties of the ice shelves themselves.

Acknowledgments

We would express sincere thanks to all the participants boarding on the Araon cruise of 2013 austral summer. This work was supported by Korea Polar Research Institute (PE18030). Most sincere appreciation should be given to the captain of the Araon, Bong Wook Kim. Without his clear-sighted decision, the cruise cannot have been fruitful. We would thank Prof. Ronald Dorn and Lewis Owen for their invaluable comments on the early version of the manuscript. Two anonymous reviewers provide very constructive and helpful comments.

Appendix A. Supplementary data

Supplementary data related to this article can be found at https://doi.org/10.1016/j.quascirev.2018.04.011.

References

Anandakrishnan, S., Alley, R.B., 1997. Stagnation of ice stream C, West Antarctica by water piracy. Geophys. Res. Lett. 24, 265–268.
Anderson, J.B., Fretwell, L.O., 2008. Geomorphology of the onset area of a paleo-ice stream, marguerite bay, antarctic peninsula. Earth Surf. Process. Landforms 33, 503–512.
Arnold, J.R., 1956. Beryllium-10 produced by cosmic rays. Science 124, 584–585.
Balco, G., Schaefer, J.M., LARISSA Group, 2013. Exposure-age record of Holocene ice sheet and ice shelf change in the northeast Antarctic Peninsula. Quat. Sci. Rev. 59, 101–111.
Balco, G., Stone, J.O., Lifton, N.A., Dunai, T.J., 2008. A complete and easily accessible means of calculating surface exposure ages or erosion rates from 10 Be and 26 Al measurements. Quat. Geochronol. 3, 174–195.
Banwell, A.F., MacAyeal, D.R., Sergienko, O.V., 2013. Breakup of the Larsen B Ice Shelf triggered by chain reaction drainage of supraglacial lakes. Geophys. Res. Lett. 40, 5872–5876.
Beer, J., Siegenthaler, U., Bonani, G., Finkel, R.C., Oeschger, H., Suter, M., Wolfli, W., 1988. Information on past solar activity and geomagnetism from 10Be in the Camp Century ice core. Nature 331, 675–679.
Bentley, M.J., 1999. Volume of Antarctic ice at the Last Glacial Maximum, and its impact on global sea level change. Quat. Sci. Rev. 18, 1569–1595.
Bentley, M.J., Hodgson, D.A., Smith, J.A., Ó Cofaigh, C., Domack, E.W., Larter, R.D., Roberts, S.J., Brachfeld, S., Leventer, A., Hjort, C., 2009. Mechanisms of Holocene palaeoenvironmental change in the antarctic peninsula region. Holocene 19, 51–69.
Bourles, D., Raisbeck, G.M., Yiou, F., 1989. 10Be and 9Be in marine sediments and their potential for dating. Geochem. Cosmochim. Acta 53, 443–452.
Brachfeld, S., Domack, E., Kissel, C., Laj, C., Leventer, A., Ishman, S., Gilbert, R., Camerlenghi, A., Eglinton, L.B., 2003. Holocene history of the Larsen-A Ice Shelf constrained by geomagnetic paleointensity dating. Geology 31, 749–752.
Chmeleff, J., von Blanckenburg, F., Kossert, K., Jakob, D., 2010. Determination of the ^{10}Be half-life by multicollector ICP-MS and liquid scintillation counting. Nucl. Instruments Methods Phys. Res. Sect. B Beam Interact. Mater. Atoms 268, 192–199.
Ciais, P., Petit, J.R., Jouzel, J., Lorius, C., Barkov, N.I., Lipenkov, V., Nicolaiev, V., 1992. Evidence for an early Holocene climatic optimum in the Antarctic deep ice-core record. Clim. Dynam. 6, 169–177.
Davies, B.J., Hambrey, M.J., Smellie, J.L., Carrivick, J.L., Glasser, N.F., 2012. Antarctic peninsula ice sheet evolution during the Cenozoic Era. Quat. Sci. Rev. 31, 30–66. https://doi.org/10.1016/j.quascirev.2011.10.012.
De Rydt, J., Gudmundsson, G.H., Rott, H., Bamber, J.L., 2015. Modeling the instantaneous response of glaciers after the collapse of the Larsen B Ice Shelf. Geophys. Res. Lett. 42, 5355–5363.
Domack, E., Duran, D., Leventer, A., Ishman, S., Doane, S., McCallum, S., Amblas, D., Ring, J., Gilbert, R., Prentice, M., 2005. Stability of the Larsen B ice shelf on the antarctic peninsula during the Holocene epoch. Nature 436, 681–685.
Domack, E.W., Jacobson, E.A., Shipp, S., Anderson, J.B., 1999. Late Pleistocene–Holocene retreat of the west antarctic ice-sheet system in the Ross Sea: Part 2—sedimentologic and stratigraphic signature. Geol. Soc. Am. Bull. 111, 1517–1536.
Domack, E.W., Williams, C., 1990. Fine structure and suspended sediment transport in three Antarctic fjords. Contrib. to Antarct. Res. I 71–89.
Donahue, D.J., Linick, T.W., Jull, A.J.T., 1990. Isotope-ratio and background corrections for accelerator mass spectrometry radiocarbon measurements. Radiocarbon 32, 135–142.
Dowdeswell, J.A., Ó Cofaigh, C., Pudsey, C.J., 2004a. Continental slope morphology and sedimentary processes at the mouth of an Antarctic palaeo-ice stream. Mar. Geol. 204, 203–214.
Dowdeswell, J.A., Ó Cofaigh, C., Pudsey, C.J., 2004b. Thickness and extent of the subglacial till layer beneath an Antarctic paleo–ice stream. Geology 32, 13–16.
Evans, J., Ó Cofaigh, C., 2003. Supraglacial debris along the front of the Larsen-a ice shelf, antarctic peninsula. Antarct. Sci. 15, 503–506.
Evans, J., Pudsey, C.J., 2002. Sedimentation associated with Antarctic Peninsula ice shelves: implications for palaeoenvironmental reconstructions of glacimarine sediments. J. Geol. Soc. London 159, 233–237.
Evans, J., Pudsey, C.J., Ó Cofaigh, C., Morris, P., Domack, E., 2005. Late Quaternary glacial history, flow dynamics and sedimentation along the eastern margin of the Antarctic Peninsula Ice Sheet. Quat. Sci. Rev. 24, 741–774.
Glasser, N.F., Scambos, T.A., 2008. A structural glaciological analysis of the 2002 Larsen B ice-shelf collapse. J. Glaciol. 54, 3–16.
Goel, P.S., Kharkar, D.P., Lal, D., Narsappaya, N., Peters, B., Yatirajam, V., 1957. The beryllium-10 concentration in deep-sea sediments. Deep Sea Res. 4, 202–210.
Graly, J., 2011. Interpretation of Meteoric 10 Be in Marginal Ice-bound Sediment of the Greenland Ice Sheet. Doctoral dissertation, University of Vermont, West Greenland.
Gu, Z.Y., Lal, D., Liu, T.S., Southon, J., Caffee, M.W., Guo, Z.T., Chen, M.Y., 1996. Five million year 10 Be record in Chinese loess and red-clay: climate and weathering relationships. Earth Planet Sci. Lett. 144, 273–287.
Heisinger, B., Lal, D., Jull, A.J.T., Kubik, P., Ivy-Ochs, S., Knie, K., Nolte, E., 2002a. Production of selected cosmogenic radionuclides by muons: 2. Capture of negative muons. Earth Planet Sci. Lett. 200, 357–369.
Heisinger, B., Lal, D., Jull, A.J.T., Kubik, P., Ivy-Ochs, S., Neumaier, S., Knie, K., Lazarev, V., Nolte, E., 2002b. Production of selected cosmogenic radionuclides by muons: 1. Fast muons. Earth Planet Sci. Lett. 200, 345–355.
Heroy, D.C., Anderson, J.B., 2005. Ice-sheet extent of the antarctic peninsula region during the last glacial maximum (LGM)—Insights from glacial geomorphology. Geol. Soc. Am. Bull. 117, 1497–1512.
Hippe, K., Kober, F., Baur, H., Ruff, M., Wacker, L., Wieler, R., 2009. The current performance of the in situ 14 C extraction line at ETH. Quat. Geochronol. 4, 493–500.
Hodgson, D.A., Bentley, M.J., Roberts, S.J., Smith, J.A., Sugden, D.E., Domack, E.W., 2006. Examining Holocene stability of antarctic peninsula ice shelves. Eos, Trans. Am. Geophys. Union 87, 305–308.
Ingólfsson, Ó., Hjort, C., Humlum, O., 2003. Glacial and climate history of the antarctic peninsula since the last glacial maximum. Arctic Antarct. Alpine Res. 35, 175–186.
Jeong, A., Seong, Y.B., Balco, G., Kim, G.T., Lee, J. Il, Yoo, K.-C., Yoon, H. il, 2014. Two sisters tell the same experience: a tale from Larsen-B and C, Antarctica. In: The 20th International Symposium on Polar Sciences, Incheon, Korea.
Johnson, J.S., Bentley, M.J., Roberts, S.J., Binnie, S.A., Freeman, S.P.H.T., 2011. Holocene deglacial history of the northeast Antarctic Peninsula - a review and new chronological constraints. Quat. Sci. Rev. 30, 3791–3802. https://doi.org/10.1016/j.quascirev.2011.10.011.
Kim, D.E., Seong, Y.B., Byun, J.M., Weber, J., Min, K., 2016. Geomorphic disequilibrium in the Eastern Korean Peninsula: possible evidence for reactivation of a rift-flank margin. Geomorphology 254, 130–145.
Kohl, C.P., Nishiizumi, K., 1992. Chemical isolation of quartz for measurement of in-situ-produced cosmogenic nuclides. Geochem. Cosmochim. Acta 56, 3583–3587.
Korschinek, G., Bergmaier, A., Faestermann, T., Gerstmann, U.C., Knie, K., Rugel, G., Wallner, A., Dillmann, I., Dollinger, G., Von Gostomski, C.L., 2010. A new value for the half-life of 10 Be by heavy-ion elastic recoil detection and liquid scintillation counting. Nucl. Instruments Methods Phys. Res. Sect. B Beam Interact. Mater. Atoms 268, 187–191.
Lal, D., 1991. Cosmic ray labeling of erosion surfaces: in situ nuclide production rates and erosion models. Earth Planet Sci. Lett. 104, 424–439.
Lavoie, C., Domack, E.W., Pettit, E.C., Scambos, T.A., Larter, R.D., Schenke, H.-W., Yoo, K.C., Gutt, J., Wellner, J., Canals, M., 2014. Paleo-ice flow directions of the Northern Antarctic Peninsula ice sheet based upon a new synthesis of seabed imagery. Cryosphere Discuss. 8.
Lifton, N.A., Jull, A.J.T., Quade, J., 2001. A new extraction technique and production rate estimate for in situ cosmogenic 14 C in quartz. Geochem. Cosmochim. Acta 65, 1953–1969.
Maejima, Y., Matsuzaki, H., Higashi, T., 2005. Application of cosmogenic 10Be to dating soils on the raised coral reef terraces of Kikai Island, southwest Japan. Geoderma 126, 389–399.
Masson-Delmotte, V., Stenni, B., Jouzel, J., 2004. Common millennial-scale variability of Antarctic and Southern Ocean temperatures during the past 5000 years reconstructed from the EPICA Dome C ice core. Holocene 14, 145–151.
Masson, V., Vimeux, F., Jouzel, J., Morgan, V., Delmotte, M., Ciais, P., Hammer, C., Johnsen, S., Lipenkov, V.Y., Mosley-Thompson, E., 2000. Holocene climate variability in Antarctica based on 11 ice-core isotopic records. Quat. Res. 54, 348–358.
McHargue, L.R., Donahue, D., Damon, P.E., Sonett, C.P., Biddulph, D., Burr, G., 2000. Geomagnetic modulation of the late Pleistocene cosmic-ray flux as determined by 10 Be from Blake Outer Ridge marine sediments. Nucl. Instrum. Methods Phys. Res. Sect. B Beam Interact. Mater. Atoms 172, 555–561.
Merrill, J.R., Lyden, E.F.X., Honda, M., Arnold, J.R., 1960. The sedimentary geochemistry of the beryllium isotopes. Geochem. Cosmochim. Acta 18, 108–129.
Michalchuk, B.R., Anderson, J.B., Wellner, J.S., Manley, P.L., Majewski, W., Bohaty, S.,

2009. Holocene climate and glacial history of the northeastern Antarctic Peninsula: the marine sedimentary record from a long SHALDRIL core. Quat. Sci. Rev. 28, 3049–3065. https://doi.org/10.1016/j.quascirev.2009.08.012.
MIDAS Project, 2017. Larsen C responds to the calving of A68 [WWW Document]. http://www.projectmidas.org/blog/larsen-c-responds. (Accessed 30 December 2017).
Mulvaney, R., Abram, N.J., Hindmarsh, R.C.A., Arrowsmith, C., Fleet, L., Triest, J., Sime, L.C., Alemany, O., Foord, S., 2012. Recent Antarctic Peninsula warming relative to Holocene climate and ice-shelf history. Nature 489, 141–144.
Naysmith, P., 2007. Extraction and Measurement of Cosmogenic in Situ 14C from Quartz. Doctoral dissertation, University of Glasgow.
Nishiizumi, K., Imamura, M., Caffee, M.W., Southon, J.R., Finkel, R.C., McAninch, J., 2007. Absolute calibration of 10 Be AMS standards. Nucl. Instrum. Methods Phys. Res. Sect. B Beam Interact. Mater. Atoms 258, 403–413.
Ó Cofaigh, C., Davies, B.J., Livingstone, S.J., Smith, J.A., Johnson, J.S., Hocking, E.P., Hodgson, D.A., Anderson, J.B., Bentley, M.J., Canals, M., Domack, E., Dowdeswell, J.A., Evans, J., Glasser, N.F., Hillenbrand, C.D., Larter, R.D., Roberts, S.J., Simms, A.R., 2014. Reconstruction of ice-sheet changes in the antarctic peninsula since the last glacial maximum. Quat. Sci. Rev. 100, 87–110. https://doi.org/10.1016/j.quascirev.2014.06.023.
Ó Cofaigh, C., Dowdeswell, J.A., Allen, C.S., Hiemstra, J.F., Pudsey, C.J., Evans, J., Evans, D.J.A., 2005. Flow dynamics and till genesis associated with a marine-based Antarctic palaeo-ice stream. Quat. Sci. Rev. 24, 709–740.
Ó Cofaigh, C., Pudsey, C.J., Dowdeswell, J.A., Morris, P., 2002. Evolution of subglacial bedforms along a paleo-ice stream, Antarctic Peninsula continental shelf. Geophys. Res. Lett. 29.
Pigati, J.S., Lifton, N.A., Timothy Jull, A.J., Quade, J., 2010. A simplified in situ cosmogenic 14C extraction system. Radiocarbon 52, 1236.
Powell, R.D., Dawber, M., Mcinnes, J.N., Pyne, A.R., 1996. Observations of the grounding-line area at a floating glacier terminus. Ann. Glaciol. 22, 217–223.
Pudsey, C.J., Evans, J., 2001. First survey of Antarctic sub–ice shelf sediments reveals mid-Holocene ice shelf retreat. Geology 29, 787–790.
Pudsey, C.J., Murray, J.W., Appleby, P., Evans, J., 2006. Ice shelf history from petrographic and foraminiferal evidence, Northeast Antarctic Peninsula. Quat. Sci. Rev. 25, 2357–2379.
Rebesco, M., Domack, E., Zgur, F., Lavoie, C., Leventer, A., Brachfeld, S., Willmott, V., Halverson, G., Truffer, M., Scambos, T., 2014. Boundary condition of grounding lines prior to collapse, Larsen-B Ice Shelf, Antarctica. Science 345, 1354–1358.
Rignot, E., Casassa, G., Gogineni, P., Krabill, W., Rivera, A.U., Thomas, R., 2004. Accelerated ice discharge from the Antarctic Peninsula following the collapse of Larsen B ice shelf. Geophys. Res. Lett. 31.
Scambos, T., Hulbe, C., Fahnestock, M., 2003. Climate-induced ice shelf disintegration in the Antarctic peninsula. Antarct. Penins. Clim. Var. Hist. Paleoenviron. Perspect 79–92.
Scherer, R.P., Aldahan, A., Tulaczyk, S., Possnert, G., Engelhardt, H., Kamb, B., 1998. Pleistocene collapse of the West Antarctic ice sheet. Science 281, 82–85.
Shen, C., Beer, J., Kubik, P.W., Suter, M., Borkovec, M., Liu, T.S., 2004. Grain size distribution, 10Be content and magnetic susceptibility of micrometer–nanometer loess materials. Nucl. Instrum. Methods Phys. Res. Sect. B Beam Interact. Mater. Atoms 223, 613–617.
Shen, C., Beer, J., Tungsheng, L., Oeschger, H., Bonani, G., Suter, M., Wölfli, W., 1992. 10Be in Chinese loess. Earth Planet Sci. Lett. 109, 169–177.
Shepherd, A., Wingham, D., 2007. Recent sea-level contributions of the Antarctic and Greenland ice sheets. Science 315, 1529–1532.
Shepherd, A., Wingham, D., Payne, T., Skvarca, P., 2003. Larsen ice shelf has progressively thinned. Science 302, 856–859.
Shevenell, A.E., Ingalls, A.E., Domack, E.W., Kelly, C., 2011. Holocene southern ocean surface temperature variability west of the antarctic peninsula. Nature 470, 250–254.
Sjunneskog, C., Scherer, R., Aldahan, A., Possnert, G., 2007. 10 Be in glacial marine sediment of the Ross Sea, Antarctica, a potential tracer of depositional environment and sediment chronology. Nucl. Instruments Methods Phys. Res. Sect. B Beam Interact. with Mater. Atoms 259, 576–583.
Sloan, B.J., Lawver, L.A., Anderson, J.B., 1995. Seismic stratigraphy of the Larsen basin, eastern antarctic peninsula. Geol. Seism. Stratigr. Antarct. margin 59–74.
Stone, J., 1998. A rapid fusion method for separation of beryllium-10 from soils and silicates. Geochem. Cosmochim. Acta 62, 555–561.
Stone, J.O., 2000. Air pressure and cosmogenic isotope production. J. Geophys. Res. Solid Earth 105, 23753–23759.
Sugden, D.E., Balco, G., Cowdery, S.G., Stone, J.O., Sass, L.C., 2005. Selective glacial erosion and weathering zones in the coastal mountains of Marie Byrd Land, Antarctica. Geomorphology 67, 317–334.
Vaughan, D.G., Marshall, G.J., Connolley, W.M., Parkinson, C., Mulvaney, R., Hodgson, D.A., King, J.C., Pudsey, C.J., Turner, J., 2003. Recent rapid regional climate warming on the Antarctic Peninsula. Climatic Change 60, 243–274.
White, D., Fülöp, R.-H., Bishop, P., Mackintosh, A., Cook, G., 2011. Can in-situ cosmogenic 14 C be used to assess the influence of clast recycling on exposure dating of ice retreat in Antarctica? Quat. Geochronol. 6, 289–294.
White, D., Fink, D., Simon, K., Post, A., Galton-Fenzi, B., Yokoyama, Y., 2016. Geochemical and isotopic signatures of ice shelves and ice shelf circulation in marine sediments. EGU General Assembly 2016, 2016EGUGA..1811585W.
Willenbring, J.K., von Blanckenburg, F., 2010. Meteoric cosmogenic Beryllium-10 adsorbed to river sediment and soil: applications for Earth-surface dynamics. Earth Sci. Rev. 98, 105–122.